Frequency-Domain Modeling Techniques for the Scalar Wave Equation : An Introduction

Jonathan B. Ajo-Franklin
Earth Resources Laboratory
Dept. of Earth, Atmospheric, and Planetary Sciences
Massachusetts Institute of Technology
Cambridge, MA 02142

Abstract

Frequency-domain finite-difference (FDFD) modeling offers several advantages over traditional time-domain methods when simulating seismic wave propagation, including a convenient formulation within the context of wavefield inversion and a straight-forward extension for adding complex attenuation mechanisms. In this short paper we introduce the FDFD method, develop a simple solver for the scalar Helmholtz problem, and explore some possible approaches for solving large scale seismic modeling problems in the frequency domain.

1 Introduction

While many numerical schemes have been proposed for modeling seismic wave propagation, explicit time domain finite-difference (TDFD) methods, originally developed in the early 1970's (2) (1) (22), continue to enjoy enormous popularity due to their efficiency, coding simplicity, and easy parallelization using domain decomposition techniques (45) (25) (26) (36). Despite the success of TDFD, frequency-domain methods are undergoing a quiet renaissance driven by researchers interested in full waveform inversion and the accurate modeling of seismic attenuation processes. Frequency-domain finite-difference (FDFD) methods have been actively applied to the wave equation since the early 1990's (28) (32) (33) but research has been limited by difficulties in solving the resulting linear systems. For 2D problems, sparse LU decomposition (16) (10) has become the method of choice for FDFD by allowing easy computation of wavefields for multiple source locations. However, direct techniques are hobbled by their large memory requirements, a restriction which has limited their application to 2D problems. In this short tutorial document we hope to provide an introduction to frequency-domain techniques [1] for solving the wave equation, details of our initial numerical implementation of a simple scalar solver, and a road map for future research within this area.

1.1 Motivation

Our investigation of FDFD methods is largely driven by our interest in full wavefield tomographic techniques. Full wavefield tomography, while computationally expensive, provides a consistent high-resolution approach to recovering elastic and possibly visoelastic properties from seismic measurements. Traditional transmission traveltime tomography techniques are capable of recovering velocity models at resolutions near the width of the first Fresnel zone, or about $\sqrt{\lambda L}$ where λ is wavelength and L is the approximate S/R offset (47). In contrast, full wavefield tomography should allow accurate imaging of features on the order of λ, probably near $\lambda/4$; physical model experiments have convincingly demonstrated that features on this scale can be

[1] Within the family of spectral techniques we will only consider frequency-space domain approaches since frequency-wavenumber (FK) methods are typically limited to 1-D models.

mapped using such techniques (29). For most of the 1990's, full wavefield tomography was applied primarily to synthetic models (32) (33) and laboratory datasets (30) (29) (11) (46) with the exception of several high quality crosswell experiments (39) (31) . Recent increases in computational power, advancement of pre-processing techniques, and improvement of inversion strategies have finally unleashed non-linear wavefield tomography on surface 2D reflection datasets, as shown by Ravaut et.al. (34) within a crustal imaging context. Although full wavefield inversion methods are still in their infancy, the stage seems set for significant advancements in the coming years. While the wavefield inversion problem can be posed in both the time (43) (24) and frequency-domains (32), the latter approach has several advantages from both theoretical and computational perspectives.

As will to be discussed at length in the following sections, the frequency domain finite-difference method is a straight-forward technique for calculating solutions to the steady-state wave equation a.k.a. the Helmholtz equation, which in our formulation is a 2nd order elliptical PDE. The advantages of the FDFD seismic modeling approach, already mentioned within the literature (32) (33), include

Decreased Non-Linearity in the Reconstruction Problem : Spectral inversion strategies allow sequential reconstruction from low to high frequency components of the data. By using the low frequency results as starting models for later inversions, the chance of convergence to a local minimum is somewhat reduced. In the time domain, wavefield comparisons are very sensitive to cycle skipping effects since both low and high frequency components are inverted simultaneously.

Superior Description of Attenuation : Arbitrary frequency dependent attenuation mechanisms can be included at no increased computational cost by making elastic parameters complex. Likewise, the inclusion of attenuation in the inverse problem is greatly simplified. In contrast, time domain methods require convolution with a response function to model viscoelastic effects. Although the convolution operation is usually approximated through use of memory variables, representation of more complicated relaxation functions is difficult and typically requires the superposition of a large number of simpler mechanisms.

Decreased Dimension of the Data Space : If the full representation of the kernel is desired in the inverse problem, frequency domain methods are the only practical approach. Since the kernel is Model $\times$ Data in dimensions, the data axis in the time domain is # Traces $\times$ # Samples which is often on the order of 1×10^8 while the data axis in the frequency domain is # Traces $\times$ 2, a manageable size for some scenarios. One should note however that the full representation of the kernel is a luxury since it is not required for the calculation of the gradient of the misfit function.

Multi-source Modeling Using LU Decomposition : As we will describe in later sections, use of LU decomposition in FDFD methods allows the fast calculation of the wavefield due to multiple sources once an initial factorization step is completed. Memory constraints limit this technique to the 2D and 2.5D cases. For larger 3D models, iterative Krylov-type techniques are required in which case frequency domain methods loose this advantage.

Despite these advantages, frequency-domain methods also suffer from a number of weaknesses which have restricted their wide adoption. Since the Helmholtz equation is a steady-state elliptical PDE, sparse linear solvers are required, making the resulting codes considerably more complicated than the equivalent explicit time-domain modeling methods. Frequency-domain methods are also more sensitive to imperfect absorbing boundary conditions since spurious reflections cannot be removed by time windowing.

Since parallel computation is almost a prerequisite for effective modeling and inversion in three dimensions, the ability to scale techniques to large machines, such as the ACES cluster used at ERL, is crucial. Linear solvers, particularly sparse LU algorithms, are difficult to parallelize on distributed memory machines in comparison to the relatively straight forward domain decomposition techniques (45) applicable to explicit time-domain methods. In situations where memory requirements are not a significant limitation, FDFD methods can be parallelized across shot location or frequency at minimal communication cost.

While this paper focuses on frequency-domain modeling and not the wavefield tomography problem, the basic components of the inverse formulation set the stage for development of FDFD methods. We follow the

derivations of Pratt and co-authors (32) (37) whose frequency-domain schemes were inspired by the earlier time-domain techniques developed by Tarantola (43) (42). Their inversion approach is based on minimizing the L_2 norm of the waveform data residual $\Delta\Psi$ or,

$$E(\omega) \;=\; \frac{1}{2}\sum_s\sum_r \Delta\Psi^*(\mathbf{r},\mathbf{s},\omega)\,\Delta\Psi(\mathbf{r},\mathbf{s},\omega), \tag{1}$$

where ω is angular frequency and $\mathbf{r}$ and $\mathbf{s}$ are surveys source and receiver locations respectively. $\Delta\Psi$ for a source/receiver pair is simply the difference between a measured and predicted wavefield at a given frequency,

$$\Delta\Psi(\mathbf{r},\mathbf{s}) \;=\; \Psi_{calc}(\mathbf{r},\mathbf{s}) - \Psi_{obs}(\mathbf{r},\mathbf{s}). \tag{2}$$

Local minimization of 1 requires calculation of the gradient of the misfit function with respect to the model m,

$$g(\mathbf{x}) \;=\; -\nabla_m E \;=\; -\frac{\partial E}{\partial m(\mathbf{x})}, \tag{3}$$

If g can be calculated, we can iterate to find the model which minimizes 1,

$$m(\mathbf{x})^{l+1} \;=\; m(\mathbf{x})^l \;+\; \gamma^l g(\mathbf{x})^l, \tag{4}$$

where l is the iteration number and γ is a step length. This process requires an good starting model to avoid convergence to a local minimum. The substantial component of the waveform inversion process is calculation of g, which can be written as

$$g(\mathbf{x},\omega) = -\omega^2\sum_s\sum_r Re\left\{\overline{G_o}(\mathbf{x},\mathbf{s},\omega)\,\overline{G_o}(\mathbf{x},\mathbf{r},\omega)\,\Delta\Psi(\mathbf{r},\mathbf{s})\right\} \tag{5}$$

where the $\overline{G_o}$ terms are the complex conjugates of the frequency domain Green's functions for the source and receiver locations. As can be seen in equation 5, efficient computation of the two Green's functions is the core component of the wavefield inversion process. The product of the two Green's function is referred to as a *wavepath* and represents the surface over which data residuals are back projected. For a dense survey with i sources and j receivers, g requires the evaluation of $i + j$ Green's functions. Since g must be calculated at each step in the optimization and multiple frequencies must be inverted, the total modeling cost in the inversion process can be substantial. The FDFD approach is tailored specifically to calculating G_o as a function of space for a given ω and m.

In addition to creating a useful computational tool, we hope to advance the state-of-the-art by investigating techniques for solving large 2D and moderate 3D problems in the frequency domain. Since solving problems of this size is currently impossible on a typical desktop machine, we are focusing on approaches amenable to parallel implementation. In particular, we hope to examine effective preconditioners for iterative solution techniques, test currently existing parallel sparse LU solvers, and explore the possibility of steady-state calculations using TDFD methods. Promising techniques will be ported to MIT's ACES cluster, a 500+ node machine capable of solving large-scale modeling problems.

2 Problem Formulation And A Simple Implementation

In this section, we formulate the scalar Helmholtz problem and present a simple 2nd order finite-difference scheme to solve this equation in the frequency domain. We should emphasize that the scheme we present is very similar to those described by previous authors (41) (14); we consider our current implementation as a first step in developing a more modern suite of modeling codes.

We begin with the inhomogeneous constant density scalar wave equation in 2D, the simplest possible wave equation which still has practical value in seismic processing,

$$\frac{1}{c^2}\frac{\partial^2 p}{\partial t^2} = \frac{\partial^2 p}{\partial x^2} + \frac{\partial^2 p}{\partial z^2}, \tag{6}$$

where c is P-wave velocity as an implicit function of space and p is the pressure field. This formulation implicitly solves for the wavefield due to a line source extending into the z-plane in a velocity model with no variation along this axis; such a result will have the kinematics of a point source in a 2D media but different amplitudes. We will be solving the frequency domain equivalent of equation 6 commonly referred to as the scalar Helmholtz equation. Taking the temporal Fourier transform of equation 6 and exploiting the derivative theorem [2] yields

$$\frac{\omega^2}{c^2} p = \frac{\partial^2 p}{\partial x^2} + \frac{\partial^2 p}{\partial z^2} \tag{8}$$

where $\omega = 2\pi f$. By rearranging equation 8, substituting wavenumber $k = \frac{\omega^2}{c^2}$, and adding source term S to the RHS we recover the traditional form of the scalar Helmholtz equation,

$$k^2 p - \left[\frac{\partial^2 p}{\partial x^2} + \frac{\partial^2 p}{\partial z^2} \right] = -S. \tag{9}$$

Among the existing papers on frequency-domain methods within the geophysical literature, several consider the 2D constant density scalar Helmholtz problem (21) (37) (49) (46) (14) (13) with alternative formulations allowing variable densities (32) (11). Song et.al. (38) (39) developed a 2.5 D extension for equation 9 based on an explicit integration over k_y, the out-of-plane wavenumber. Song's approach allows the effective modeling of 2D reflection and crosswell experiments with the correct geometric amplitudes. To our knowledge, no 3D Helmholtz formulations have been described in the geophysical literature, probably due to prohibitive memory requirements.

2.1 Absorbing Boundary Conditions

We wish to find the solution to equation 9 for a finite model domain, Ω, but without reflected energy from the domain boundaries. For our a test implementation we use a very simple absorbing boundary condition (ABC) first proposed by Engquist and Majda (12),

$$\frac{\partial p}{\partial n} - \mathbf{i}kp = 0 \tag{10}$$

where n is the direction normal to the absorbing model boundary. For more details on the derivation of this 1st order boundary condition we refer the reader to appendix 1. In this case, the price for ABC simplicity is poor absorption of out-going waves at high incidence angles. The 1st order Engquist/Majda condition is only perfectly absorbing when the out-going wave impacts the boundary at normal incidence. More sophisticated ABCs exist including a higher-order formulation of the Engquist/Majda class of operators due to Kjartansson (23) which was implemented by Pratt (32) in the context of FDFD modeling. Although not described in the literature, sponge-type boundary conditions of the form described by Cerjan et.al. (6) have also been developed in the frequency-domain; this approach uses a tapered increase in the imaginary component of velocity near the domain boundaries to absorb out-going waves. The most recent advance in ABC theory is the so-called Perfectly Matched Layer (PML) technique proposed by Berenger (5) which requires a wave equation with a split pressure term but offers an almost complete elimination of boundary reflections. Both Dessa and Pascal (11) and Hustedt et.al. (20) have successfully implemented the PML within FDFD solvers.

2.2 Discretization

We discretize equation 9 using an implicit finite difference scheme based on 2nd order accurate centered difference operators. All derivations are based on use of a 2D rectalinear mesh with constant grid spacings in both the x and z directions. Local references to discrete locations on the grid are made through subscripts i

[2]
$$\frac{d^n}{dt^n} f(t) \rightleftharpoons (2\pi i f)^n F(s) \tag{7}$$

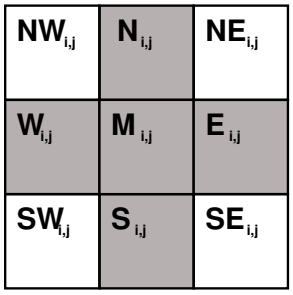

Figure 1: Symbolic abbreviations for element locations on a 9 point 2D FD stencil.

and j. Any given mesh has $m \times n$ total samples. We assume a left-handed coordinate system with positive z oriented down (i.e. depth). The centered difference operator for the second derivative can be written as,

$$\frac{\partial^2 p}{\partial x^2} = \frac{p_{i-1,j} - 2p_{i,j} + p_{i+1,j}}{\Delta x^2} \tag{11}$$

where Δx is the grid spacing in the x direction on our spatial mesh. Substituting our difference operators 11 into equation 9 and discretizing all parameters in local indicial notation yields,

$$\frac{\omega^2}{c^2} p_{i,j} + \left[\frac{p_{i-1,j} - 2p_{i,j} + p_{i+1,j}}{\Delta x^2}\right] + \left[\frac{p_{i,j-1} - 2p_{i,j} + p_{i,j+1}}{\Delta z^2}\right] = -S_{i,j}. \tag{12}$$

Since we wish to solve equation 12 implicitly, we group terms by grid location and solve for the coefficient set which operates on $p_{i,j}$. Figure 1 shows our symbolic convention for these coefficients which uses abbreviations for the different cardinal directions.
Using this syntax we can write the coefficients for interior mesh locations $[i \to 2, n-1]$ $[j \to 2, m-1)]$ as,

$$\begin{array}{rcl} M_{i,j} & = & \frac{\omega^2}{c^2_{i,j}} - 2\left(\frac{1}{\Delta x^2} + \frac{1}{\Delta z^2}\right) \\ E_{i,j} & = & \frac{1}{\Delta x^2} \\ W_{i,j} & = & \frac{1}{\Delta x^2} \\ N_{i,j} & = & \frac{1}{\Delta z^2} \\ S_{i,j} & = & \frac{1}{\Delta z^2} \end{array} \tag{13}$$

At the boundary of the computational domain, we discretize the Engquist/Majda ABC from equation 10. To handle the spatial derivative at the mesh boundary, we use a 1st order forward difference operator of the form,

$$\frac{\partial p}{\partial x} = \frac{p_{i+1} - p_i}{\Delta x}. \tag{14}$$

For the case of the top boundary where $j = 1$, we can then write the discrete form of the ABC as,

$$\frac{p_{i,2} - p_{i,1}}{\Delta z} + \mathbf{i}\frac{\omega}{c_{i,1}} = 0. \tag{15}$$

Following our treatment of the interior points, we can then write the equivalent stencil values for the top boundary as,

$$\begin{array}{rcl} M_{i,j} & = & -\frac{1}{\Delta z} - \mathbf{i}\frac{\omega}{c_{1,j}} \\ E_{i,j} & = & 0 \\ W_{i,j} & = & 0 \\ N_{i,j} & = & 0 \\ S_{i,j} & = & \frac{1}{\Delta z} \end{array} \tag{16}$$

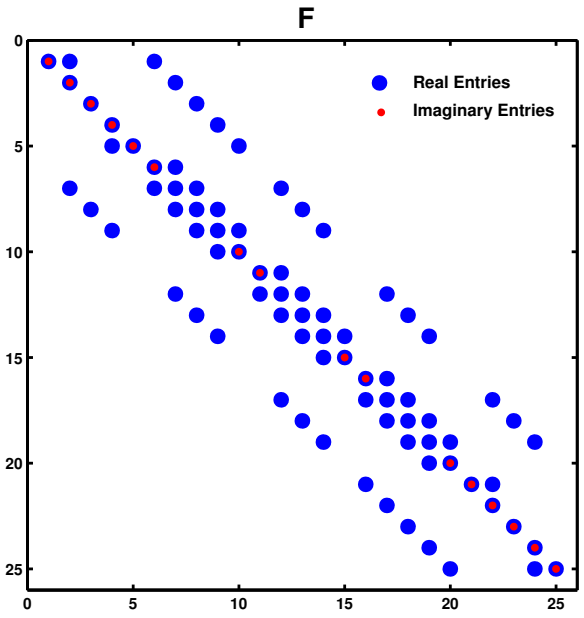

Figure 2: The sparsity pattern of operator F for a toy 5×5 problem.

Appendix 2 provides our full discretized formulation for the domain interior, edges, and corners. The discrete problem can then be described in terms of the differential operator F which includes all velocity variations, the complex pressure field u, and a source term, s,

$$Fu = -s \tag{17}$$

In equation 17, 2D locations from the FD stencils are mapped to 1D index k using $k = (i-1)N + j$; each 2D stencil maps to a column in F. As discussed previously, all boundary conditions are included in F.

Before discussing solution techniques we should summarize the properties of the Helmholtz operator matrix, F, so as to constrain the class of applicable approaches. The statements below, while tailored particularly to our discrete formulation, are typical of implicit frequency-domain formulations.

F is sparse and square : The structure of F is quite sparse, particularly when a 2nd order operator is used to estimate spatial derivatives. All entries are on 5 diagonals with exactly $5mn - 6(m+n) + 16$ non-zero values within an $mn \times mn$ square matrix.

F is complex : For the case of non-attenuating media, the only complex entries in F are due to the absorbing boundary conditions. In the more general case, any c value might be complex. In either case, all complex values are confined to the central diagonal, F_{ii}.

F is non-symmetric : Although the interior FD stencils are symmetric, the one-sided differences used in the ABC produce asymmetry in the operator.

F is indefinite : Typically, F has both positive and negative eigenvalues.

Figure 2 shows a more concrete representation of the sparsity pattern of the Helmholtz operator matrix for a toy 5×5 problem; blue circles represent elements with real components while red circles denote the existence of imaginary components. F is "block tridiagonal with fringes" in the common matrix parlance. To generate an accurate solution for equation 17, the pressure field must be discretized finely enough to avoid significant numerical dispersion. Typically a spacing constraint of $\Delta x < \lambda/12$ is used for second-order

schemes. In TDFD codes for solving the scalar wave equation, schemes as high as 8th or 10th order in space are routinely used (7) to relax spacing constraints to as low as $\Delta x < \lambda/3$. In the frequency-domain, traditional high order spatial derivatives increase the bandwidth of F making efficient solution of equation 17 difficult. This limitation has motivated the development of compact FD stencils (9 pnts in 2D) which preserve the bandwidth of F while offering better dispersion properties in comparison to the standard 2nd order scheme. Jo et.al. (21) proposed such a compact stencil, derived by considering the weighted average of a regular and a rotated 5 point operators. They determined the weighting coefficients for the two stencils by solving an optimization problem in terms of the resulting dispersion relationships. Stekl and Pratt (40) derive a similar set of stencils for the 2D elastic Helmholtz equation; they argue that the use of higher-order methods with stencils larger than 9 points is not practical due to increased memory requirements. These compact 9-point stencils are now considered the state-of-the-art for scalar FDFD solvers (11).

3 Methods of Solving The Discrete Helmholtz System

A variety of methods have been proposed to solve the system $Fu = -s$, each with different computational advantages. We will focus on sparse LU decomposition algorithms, the most popular approach for solving the discrete Helmholtz problem (40) (29) (11) (20) (34) (46) although we will also touch on iterative (27) (14) (13) (15) (41), dual-solver (19), and steady-state TDFD techniques which are a topic of current interest in the research community.

3.1 Direct Methods : Sparse LU Decomposition

LU factorization is one of the most popular direct techniques for solving linear systems and is both stable and efficient for a variety of problems. Given a system $A\,x = b$, LU techniques factor A into upper and lower triangular matrices such that $A = L\,U$. Solving for x typically occurs in three steps,

$$\begin{array}{lcll} A & \Rightarrow & L\,U & (factorization) \\ L\,y & = & b & (forward\ substitution) \\ U\,x & = & y & (back\ substitution) \end{array} \tag{18}$$

The factorization step is $O(n^3)$ in the number of equations while both the forward and back substitution steps are $O(n^2)$ since L and U are triangular. As can be seen from sequence 18, since the factorization is independent of b, once L and U are computed, a variety of different RHS can be solved for at a cost of $O(n^2)$. In the seismic modeling case, this means that once the Helmholtz operator, F, is factored, we can cheaply compute the wavefield for a large number of source positions at low cost.

An important fact to note is that while F is very sparse in our case, there is no guarantee that the resulting factors will have a similar number of non-zero entries. Due to this in-fill process, application of LU decomposition to the frequency domain modeling problem requires careful consideration of memory constraints. In the worst case, the LU factorization process will result in non-zero values for all entries within the band outlined by the stencil; for a 2nd order 2D FD operator this amounts to $n \times 2(m^2 + m)$ entries in the LU factors in comparison to the $5mn - 6(m + n) + 16$ entries in the original operator matrix. If we assume that $m = n$ then the storage required for the operator is asymptotically $O(n^2)$ in comparison to the $O(n^3)$ required for the band-limited LU factors. Pratt and co-authors (32) (33) (28) (30) used a combination of a commercial band-limited LU factorization code (FMSLIB) and dedicated hardware (a FPS-164/MAX matrix accelerator) to solve a series of small test problems but their early approach has an $O(n^3)$ storage requirement and does not scale to larger problems.

Luckily, powerful methods for preserving the sparsity of L and U have been developed; all of these techniques are based on pre-ordering the rows and columns of A in order to insure that minimal in-fill occurs in the factorization step. Instead of $A = LU$ we can solve the system,

$$P_r\,A\,P_c = L\,U \tag{19}$$

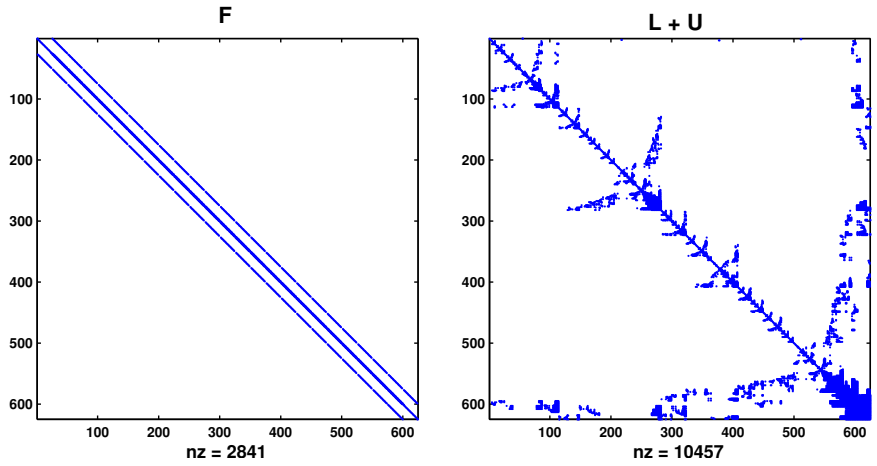

Figure 3: Above, the sparsity pattern of operator F and the result of LU factorization using COLAMD (UMFPACK 4.4). Note the increase in number of non-zero element and the related loss of structure.

where P_r and P_c are row and column permutation matrices. Although determination of the optimal sparsity-preserving permutation is an NP-complete problem (48), several algorithms exist based on either local or global heuristics. Popular approaches for computing the appropriate permutation matrices include nested dissection (16), multiple minimum degree ordering [MMD] (17), approximate minimum degree ordering [AMD] (4), and column approximate minimum degree ordering [COLAMD] (9). Nested dissection in particular has seen wide application within the frequency-domain modeling community (40) (29) (46) but generally requires a problem-specific ordering component making stencil modification somewhat more difficult. The best bound on storage for the 2D sparse LU problem (40) using a nested dissection ordering is $O(n^2 \log n)$, a significant improvement over the $O(n^3)$ storage required for the standard band-limited factorization.

Among the more recent studies, Dessa and Pascal (11) use the sparse LU factorization code MA41, part of the Harwell Subroutine Library (HSL), to solve the scalar Helmholtz problem. Ma41 uses the AMD algorithm for determining a set of in-fill reducing column permutations. They claim that the resulting LU factors have in-fill levels similar to those generated by problem-specific nested dissection approaches.

Figure 3 shows an example of the effects of factorization process on the sparsity and structure of L and U when using COLAMD ordering approach implemented in UMFPACK. Figure 4 shows the rate at which the memory requirements of the sparse factorization grows as a function of problem size for this particular ordering. The blue curve shows the size of the operator F if stored explicitly while the red curve shows the size of the L and U factors combined. As is clear from the plot, the size of the factors grows considerably faster than F, which is linear in the number of grid samples ($M \times N$).

3.1.1 Existing Solvers

Since the development of efficient sparse LU solvers is a highly specialized field, we are currently using several off-the-shelf codes for solving our modeling problems. We are testing Demmel et.al's SuperLU (10) , Davis and Duff's UMFPACK (8), Amestoy et.al.'s MUMPS, (3), and Gupta's Watson Sparse Matrix Package (WSMP) (18). Within the recent FDFD literature, UMFPACK (20) (34) and MUMPS (19) have been the predominant sparse LU solvers.

Gupta (18), the author of WSMP, provides a performance comparison of several modern sparse direct solvers including WSMP, SuperLU, UMFPACK 3.2, and MUMPS. He concludes that WSMP is the most efficient solver for a variety of problems with MUMPS ranking second among the codes analyzed. However, his suite of test matrix does not include an FD problem similar to our Helmholtz system so the applicability of his conclusions are unclear.

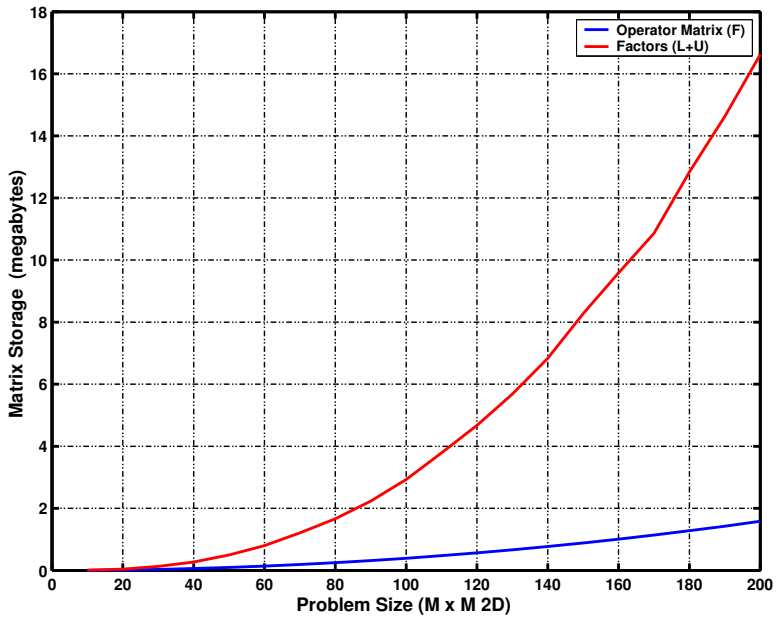

Figure 4: Above, the required storage for F vs. L+U for a square M x M problem. Sparse factorizations were calculated with COLAMD (UMFPACK 4.4).

3.2 Iterative And Dual-Method Techniques

Iterative techniques for solving the Helmholtz equation lack the advantages of sparse LU decomposition when applied to multi-source problems. However, as problem size increases, iterative techniques gain the upper hand due to their more modest memory requirements. In general, iterative Krylov algorithms such as BICGSTAB (44) and General Minimum Residual (GMRES) (35) require $O(n^2)$ storage in 2D and $O(n^3)$ in 3D; for significant 3D problems, sparse LU decomposition's memory requirements, even with smart in-fill reduction, become prohibitively expensive, $O(n^4)$, and iterative techniques must be adopted. In addition to lower storage costs, iterative methods are often easy to parallelize in comparison to sparse LU solvers, making them an appealing alternative for large scale problems. Unfortunately, Krylov techniques which use traditional preconditioners e.g. ILU, often exhibit very slow convergence rates on Helmholtz problems making development of a good preconditioner essential.

Multigrid methods, which are among the most effective class of preconditioners for Laplace and Poisson problems, are often difficult to apply to the Helmholtz equation. The basic multigrid approach computes a relatively smooth solution on a coarse mesh and then sequentially refines the mesh to calculate components with higher wavenumbers. In the case of the Helmholtz problem, coarse mesh solutions do not sufficiently sample the wavefield e.g. $\Delta x < \lambda/15$, and suffer from extreme dispersion effects making the refinement process problematic. Plessix and Mulder (27) examine a separation-of-variables (SOV) preconditioner with the BICGSTAB algorithm to solve the Helmholtz problem but conclude that SOV fails as velocity models become increasingly rough. Erlangga et.al. (14) (13) describes application of a preconditioner related to the complex shifted Laplace (CSL) problem coupled to a restarted GMRES code to solve the Helmholtz equation. Tang (41) explores both CSL,, and combined CSL/SOV preconditioners. He concludes that none of the methods are sufficient for the solution of large scale problems and that the combined CSL/SOV preconditioner does not significantly improve performance. In light of these previous studies, the development of a high-performance preconditioner for the scalar Helmholtz equation is still an open problem.

Hustedt et.al. (19) recently developed a dual-method approach which uses a sparse LU solver to calculate an approximate solution on a coarse grid; this solution is then used as a starting guess for an iterative

solution calculated on a finer mesh. While their approach has not yet been applied to the 3D case, a dual direct/iterative approach may circumvent some of the convergence problems observed with purely iterative schemes.

We have selected Sandia National Laboratory's AZTEC package as a starting point for developing parallel iterative techniques for solving the Helmholtz problem. AZTEC supports GMRES and BICGSTAB in addition to a wide variety of parallel preconditioners. AZTEC has been successfully scaled to PC clusters with 1000's of nodes and can also take advantage of SuperLU for parallel generation of incomplete LU preconditioners. Although we have not yet integrated AZTEC into our prototype FDFD solver, we hope to have a system for iteratively solving the Helmholtz equation within the coming months.

3.3 Computing Frequency Domain Solutions In Time

A final approach which we are considering is the calculation of frequency-domain Green's functions in the time-domain by driving an explicit FDTD solver to steady state with a monochromatic source function. The difficulty of this approach is developing a strategy for efficiently extracting the phase and amplitude of the complex wavefield without having to store the time history of every point within the model.

4 Current Implementation Framework

Up to this point we have neglected to mention details of how individual components of our frequency-domain modeling system are implemented and combined. We have adopted a modular approach to allow easy modification of either the FD implementation or the solver. Figure 5 shows the primary computational components included in our system. Most of these elements have already been connected but the design is not yet complete.

The entire modeling process is driven by a MATLAB interface which uses temporary transfer files and system calls to invoke the more computationally intensive codes. The linear system generator was written in C++ and generates an intermediate file containing all of the non-zero components of the operator matrix F. This intermediate file can be directly loaded into MATLAB to examine structure or converted to a column-compressed Harwell/Boeing file, a format directly supported by most sparse solver packages. At the solver stage, the user can select between either one of the pre-conditioned iterative solvers used within AZTEC or one of the four sparse LU solvers that we are investigating. The resulting set of complex wavefields will then be loaded into a future wavefield tomography system or combined (over frequency) and Fourier transformed to generate a time-domain synthetic wavefield. We used the UMFPACK 4.4 sparse LU solver for most of our initial numerical experiments.

Since a key aspect of our future work involves the inversion of substantial 2D and small 3D datasets, we have focused on solvers with parallel implementations which we are currently porting to the ACES computational cluster. SuperLU, MUMPS, WSMP, and AZTEC are the most likely candidate packages for a future parallel modeling system.

5 Initial Examples

Although our FDFD system is still immature, we have generated some initial test examples using the simple scheme detailed in previous sections. Figure 6 depicts calculation of the scattered wavefield due to a high velocity perturbation (the ERL logo) at two different frequencies (left column, 800 Hz, right column 400 Hz). The top row shows the real component of the complex wavefield, G_0, due to a line source (red star) in a homogeneous background media ($V_p = 1500$ m/s) sampled on a 400×300 grid with $\Delta x = \Delta z = 0.11$m. Waves reflected from the domain boundary, due to our naive ABC, are visible at the top right and top left of the wavefield as low amplitude oscillations. The middle row shows a recalculation of the wavefield, G_1, where the model includes a high velocity ($V_p = 2000$ m/s) perturbation in the form of the ERL logo. The bottom row shows the scattered wavefield due to the logo, $G_{scat} = G_1 - G_0$. Both forward and back

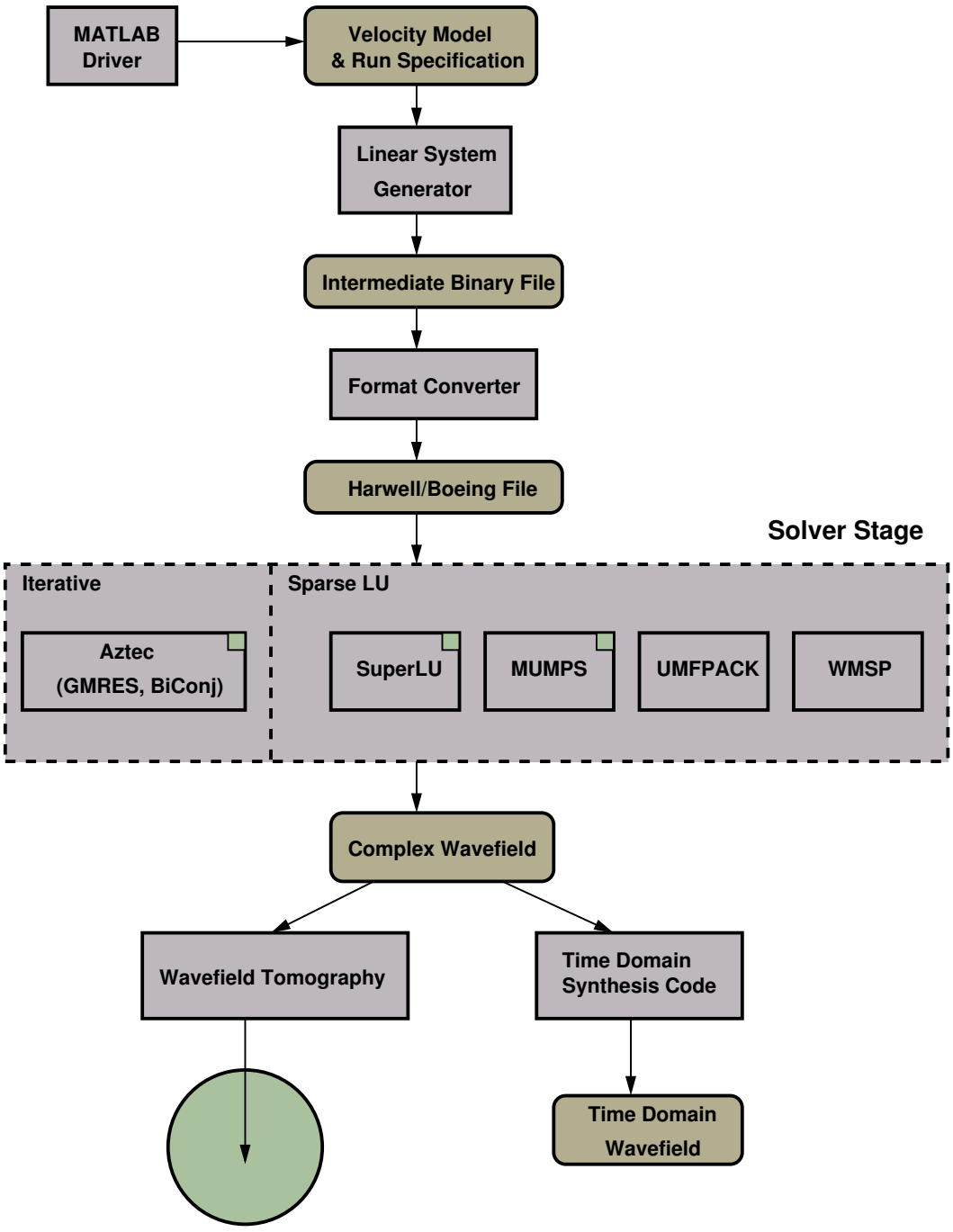

Figure 5: Implementation components for our frequency-domain modeling system.

scattered energy are visible. All wavefields were calculated using UMFPACK 4.4's sparse LU solver with the COLAMD ordering.

Figure 7 shows a second example demonstrating the potential application of FDFD for computing the gradient of the frequency-domain waveform tomography problem. As was previously shown in equation 5, the core component of the frequency-domain gradient is the product of the complex conjugate of two Green's functions, corresponding to wavefields generated by a source at location $\mathbf{s}$ and a second source located at the receiver location, $\mathbf{r}$. The left column shows the evaluation of this wavepath, $\overline{G_o}(\mathbf{x},\mathbf{s},\omega)\,\overline{G_o}(\mathbf{x},\mathbf{r},\omega)$, for a homogeneous background medium with the first, second, and third rows corresponding to the source, receiver, and product Green's functions respectively. The right column depicts the equivalent set of calculations for the ERL perturbed model. The mesh dimensions and velocity models are identical to those used in the previous example. Reflected arrivals from the imperfect ABC are particularly visible in the gradient images on the bottom row where they manifest as an irregular roughness within the inner Fresnel zone.

Figure 8 shows the 10 Hz Green's function for the popular Marmousi velocity model, a synthetic developed from studies in Angola's Cuanza Basin. The "hard" interface version of this model was sampled on a 768 $\times$ 244 mesh, dimensions on par with some of the largest seismic problems solved by FDFD in the open literature.

6 The Way Forward

In this short paper we have introduced the frequency-domain finite-difference method, reviewed several current techniques for solving the FDFD problem, and developed a simple 2D scalar Helmholtz forward modeling code. Considering the high computational cost of moving to 3D modeling using FDFD, the outstanding problem confronting us is scaling existing approaches to large parallel machines. Sparse LU methods, although ideally suited for 2D multi-source problems, will probably only be useful for small 3D problems due to their $O(n^4)$ storage requirements. However, in many cases the 2.5D approximation may be sufficient for effective modeling, particularly for crosswell and densely sampled, long-offset surface surveys. Large scale modeling will probably require the adoption of either iterative Krylov-type solvers or the calculation of frequency domain responses using a steady-state explicit TDFD approach, both of which require $O(n^3)$ storage.

Our next step will be revision of our FDFD code to include better ABCs and a more sophisticated 4th order compact Laplacian stencil (21) for calculation of spatial derivatives. Once these modifications are complete the more interesting problems related to solving the Helmholtz system and wavefield tomography problems can be considered.

An Effective Preconditioner : The development of effective preconditioners for the Helmholtz problem seems to be the most significant challenge to the FDFD method. We are actively exploring the use of physics-based preconditioners based on asymptotic approximations to the wave equation, an approach which has not yet been considered in the literature. If an effective strategy can be developed we will port the resulting code to the ACES cluster for the solution to large modeling tasks.

Steady-state TDFD ? : Easy parallelization and an $O(n^3)$ memory footprint may make the steady-state TDFD approach competitive with iterative solvers. We are considering adaptation of existing TDFD codes for this type of calculation, again on the ACES cluster. Since the existing TDFD codes are already parallelized using domain-decomposition, the primary challenge is the effective extraction of steady-state phase and amplitudes from the resulting waveforms without storing the recorded signal at all times.

Parallel Sparse-LU : Even though sparse LU solvers will probably not effectively scale to large 3D problems, they remain an excellent choice for 2D and 2.5D problems, particularly if parallelization allows scaling to reasonably large models. We will investigate several existing sparse LU solvers to accomplish this task including SuperLU, MUMPS, and WSMP.

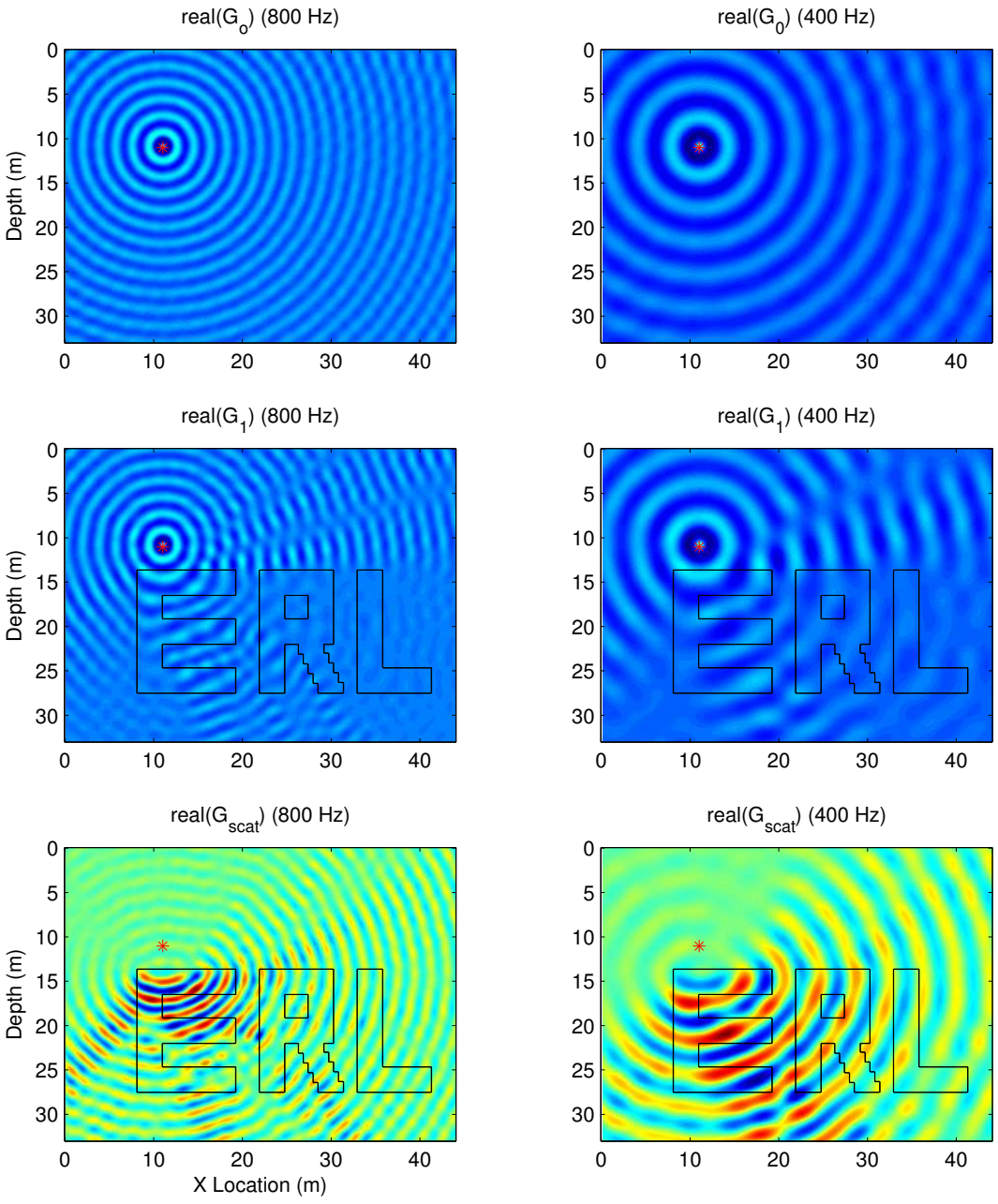

Figure 6: 800 Hz and 400 Hz solutions for a 400 x 300 test model. The top row shows the real part of the complex wavefield for the homogeneous case, while the middle and bottom rows show the wavefield perturbed by the ERL logo and the resulting scattered components of the wavefield.

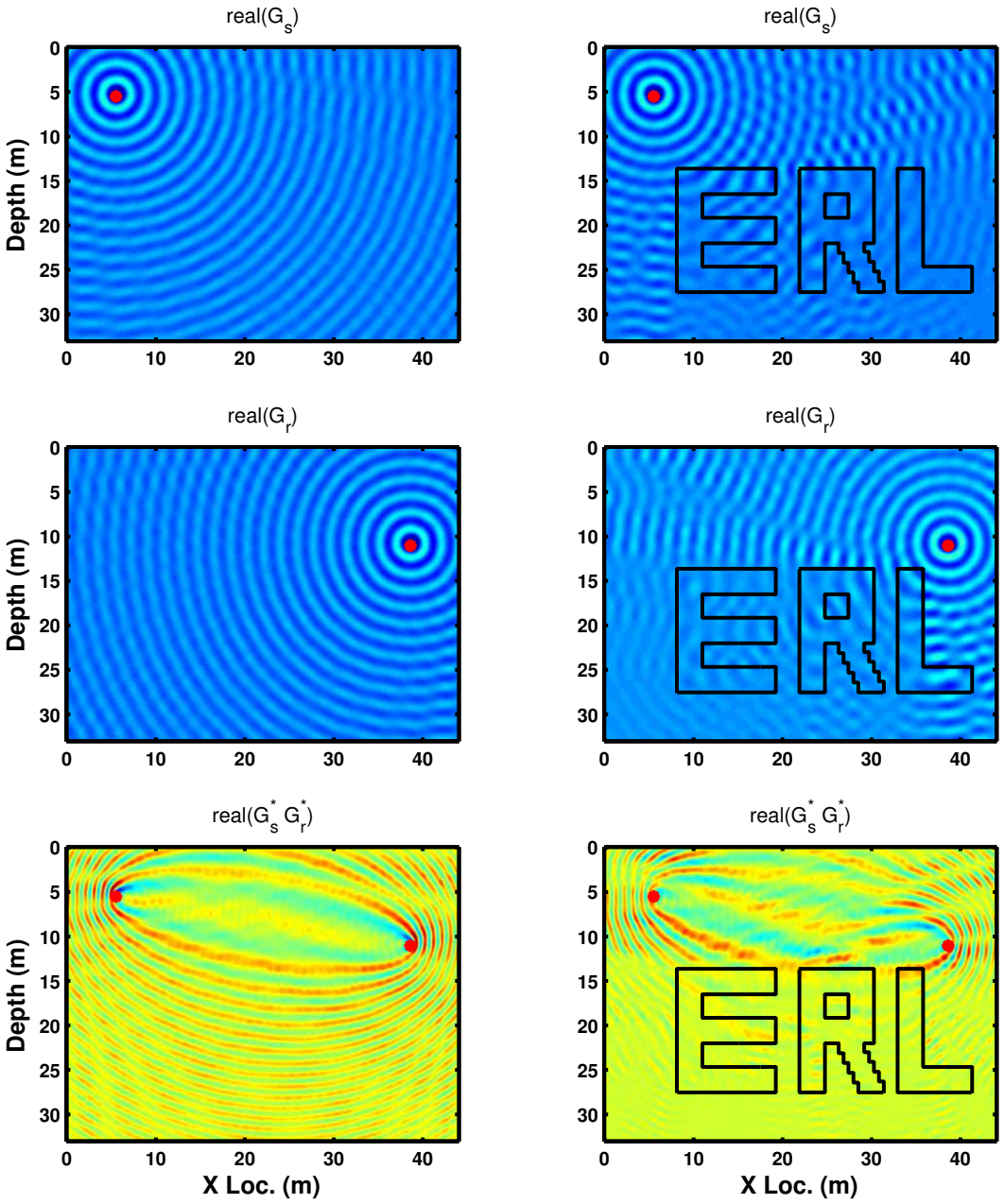

Figure 7: Frequency domain gradient calculations for homogeneous (left column) and inhomogeneous (right) models. The top row depict the source Green's functions, the middle row show the receiver Green's functions, and the bottom shows the monochromatic wavepath (misfit gradient component) for the same S/R pair.

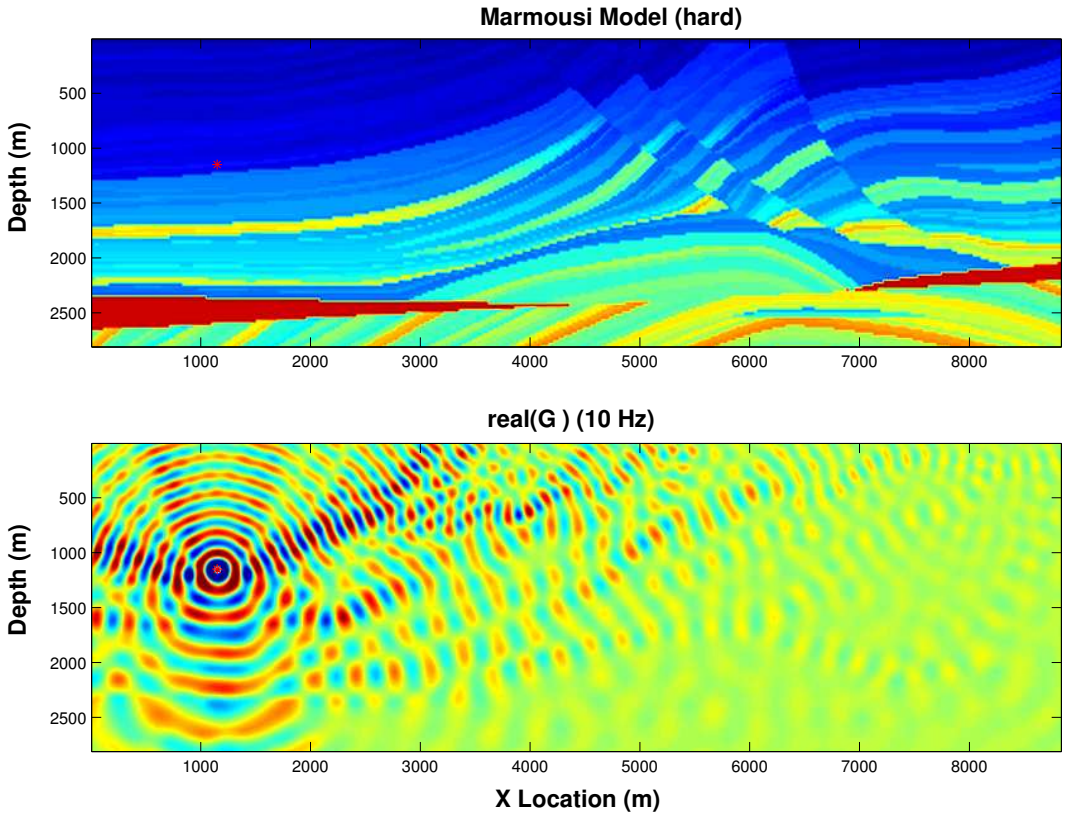

Figure 8: Example of a 10 Hz monochromatic wavefield for a 768×244 sample version of the Marmousi model. The red star indicates the source location.

FD Wavefield Tomography With Attenuation : The most interesting problem is not the FDFD problem in itself, but application of the resulting frequency-domain Green's functions to the wavefield inversion problem. Our ultimate goal is the development of a system for the regularized inversion of full waveform data with a focus on extracting Q from borehole seismic surveys.

7 Acknowledgments

We would like to thank the ERL Founding Members consortium for their generous support.

A The Engquist-Majda Absorbing Boundary Condition

Engquist and Majda (12) derived one of the simplest absorbing boundary conditions through application of a one-way wave equation at domain boundaries. They first considered equation 6 in terms of a differential operator of the form,

$$L = \frac{\partial^2}{\partial x^2} + \frac{\partial^2}{\partial z^2} - \frac{1}{c^2}\frac{\partial^2}{\partial t^2} = D_x^2 + D_z^2 - \frac{1}{c^2}D_t^2. \tag{20}$$

Equation 6 can then be written in terms of operator 20 as $LP = 0$ where P is the pressure field. Operator L can be factored into in-going and out-going components such that $LU = L^+L^-U = 0$ where the two factors are written as

$$L^+ = D_x + \frac{D_t}{c}\sqrt{1-S^2} \tag{21}$$

$$L^- = D_x - \frac{D_t}{c}\sqrt{1-S^2} \tag{22}$$

where $S = \frac{D_z c}{D_t}$. When operator 22 is applied at the left boundary of the computational domain ($x = 0$), waves approaching at any angle are absorbed. However, the existence of a square root operator prevents straight forward implementation of equations 21 and 22. The common solution to this difficulty is to use a Taylor series approximation to $\sqrt{1-S^2}$. The single term approximation derived in this manner is then

$$\sqrt{1-S^2} \approx 1 \tag{23}$$

which when substituted into operator L^- yields

$$L^- \approx D_x - \frac{D_t}{c}. \tag{24}$$

$$L^-P = \frac{\partial p}{\partial x} - \frac{1}{c}\frac{\partial p}{\partial t} \tag{25}$$

To generate our frequency domain boundary condition we apply a temporal Fourier transform to equation 25,

$$\frac{\partial p}{\partial x} - ikp = 0. \tag{26}$$

which can be written more generally as

$$\frac{\partial p}{\partial n} - ikp = 0. \tag{27}$$

where n is simply the normal direction with respect to the appropriate domain boundary ($\partial\Omega$). While the first order Engquist-Majda operator is extraordinarily simple to implement, it only perfectly absorbs planewaves that are normally incident to the domain boundary. Higher order expansions for $\sqrt{1-S^2}$ yield lower reflectivities at grazing incident angles but also increase the size and complexity of the resulting finite difference operators.

B Full Problem Discretization

In section 2.2 we introduced the 9 point 2D star used for discretizing the Helmholtz operator and wrote the explicit formulation for the domain interior and the top boundary. We now present the complete coefficient set including all boundaries and corners. As mentioned previously, the 1st order Engquist-Majda ABC is far from perfect and a serious implementation should consider replacement with either a higher-order ABC or some type of PML-based absorbing region. Additionally, the stencils that we use at corner locations are very naive; they are simply the sum of the two orthogonal boundary stencils. A better implementation would consider the corners in a rotated coordinate frame so that $\frac{\partial p}{\partial n}$ is at 45 degrees from either grid axis.

B.1 Domain Interior $[i \rightarrow 2, n-1]\,[j \rightarrow 2, m-1)]$

$$\begin{array}{rcl} M_{i,j} & = & \frac{\omega^2}{c_{i,j}^2} - 2\left(\frac{1}{\Delta x^2} + \frac{1}{\Delta z^2}\right) \\ E_{i,j} & = & \frac{1}{\Delta x^2} \\ W_{i,j} & = & \frac{1}{\Delta x^2} \\ N_{i,j} & = & \frac{1}{\Delta z^2} \\ S_{i,j} & = & \frac{1}{\Delta z^2} \end{array} \tag{28}$$

B.2 Top Boundary $[i \rightarrow 2, n-1]\,[j \rightarrow 1)]$

$$\begin{array}{rcl} M_{i,j} & = & -\frac{1}{\Delta z} - \mathbf{i}\frac{\omega}{c_{i,1}} \\ E_{i,j} & = & 0 \\ W_{i,j} & = & 0 \\ N_{i,j} & = & 0 \\ S_{i,j} & = & \frac{1}{\Delta z} \end{array} \tag{29}$$

B.3 Bottom Boundary $[i \rightarrow 2, n-1]\,[j \rightarrow m)]$

$$\begin{array}{rcl} M_{i,j} & = & -\frac{1}{\Delta z} - \mathbf{i}\frac{\omega}{c_{i,m}} \\ E_{i,j} & = & 0 \\ W_{i,j} & = & 0 \\ N_{i,j} & = & \frac{1}{\Delta z} \\ S_{i,j} & = & 0 \end{array} \tag{30}$$

B.4 Right Boundary $[i \rightarrow 1]\,[j \rightarrow 2, m-1)]$

$$\begin{array}{rcl} M_{i,j} & = & -\frac{1}{\Delta x} - \mathbf{i}\frac{\omega}{c_{1,j}} \\ E_{i,j} & = & 0 \\ W_{i,j} & = & \frac{1}{\Delta x} \\ N_{i,j} & = & 0 \\ S_{i,j} & = & 0 \end{array} \tag{31}$$

B.5 Left Boundary $[i \rightarrow n]\,[j \rightarrow 2, m-1)]$

$$\begin{array}{rcl} M_{i,j} & = & -\frac{1}{\Delta x} - \mathbf{i}\frac{\omega}{c_{n,j}} \\ E_{i,j} & = & \frac{1}{\Delta x} \\ W_{i,j} & = & 0 \\ N_{i,j} & = & 0 \\ S_{i,j} & = & 0 \end{array} \tag{32}$$

B.6 Top Right Corner $[i \rightarrow n]\,[j \rightarrow 1)]$

$$\begin{array}{lcl} M_{i,j} & = & -\frac{1}{\Delta x} - \frac{1}{\Delta z} - 2\mathbf{i}\frac{\omega}{c_{n,1}} \\ E_{i,j} & = & 0 \\ W_{i,j} & = & \frac{1}{\Delta x} \\ N_{i,j} & = & 0 \\ S_{i,j} & = & \frac{1}{\Delta z} \end{array} \tag{33}$$

B.7 Top Left Corner $[i \rightarrow 1]\,[j \rightarrow 1)]$

$$\begin{array}{lcl} M_{i,j} & = & -\frac{1}{\Delta x} - \frac{1}{\Delta z} - 2\mathbf{i}\frac{\omega}{c_{1,1}} \\ E_{i,j} & = & \frac{1}{\Delta x} \\ W_{i,j} & = & \\ N_{i,j} & = & 0 \\ S_{i,j} & = & \frac{1}{\Delta z} \end{array} \tag{34}$$

B.8 Bottom Right Corner $[i \rightarrow n]\,[j \rightarrow m)]$

$$\begin{array}{lcl} M_{i,j} & = & -\frac{1}{\Delta x} - \frac{1}{\Delta z} - 2\mathbf{i}\frac{\omega}{c_{n,m}} \\ E_{i,j} & = & 0 \\ W_{i,j} & = & \frac{1}{\Delta x} \\ N_{i,j} & = & \frac{1}{\Delta z} \\ S_{i,j} & = & 0 \end{array} \tag{35}$$

B.9 Bottom Left Corner $[i \rightarrow 1]\,[j \rightarrow m)]$

$$\begin{array}{lcl} M_{i,j} & = & -\frac{1}{\Delta x} - \frac{1}{\Delta z} - 2\mathbf{i}\frac{\omega}{c_{1,m}} \\ E_{i,j} & = & \frac{1}{\Delta x} \\ W_{i,j} & = & 0 \\ N_{i,j} & = & \frac{1}{\Delta z} \\ S_{i,j} & = & 0 \end{array} \tag{36}$$

References

[1] Alford, R., and amd D.M. Boore, K. K. Accuracy of finite-difference modeling of the acoustic wave equation. *Geophysics 39*, 6 (1974), 834–842. 1

[2] Alterman, Z., and Karal, F. Propagation of elastic waves in layered media by finite-difference methods. *Bulletin of the Seismological Society Of America 58*, 1 (68), 367–398. 1

[3] Amestoy, P., Duff, I., Koster, J., and L'Excellent, J.-Y. A fully asynchronous multifrontal solver using distributed dynamic scheduling. *SIAM Journal of Matrix Analysis and Applications 23*, 1 (2001), 15–41. 8

[4] Amestoy, P. R., Davis, T. A., and Duff, I. S. An approximate minimum degree ordering algorithm. *SIAM Journal on Matrix Analysis and Applications 17*, 4 (1996), 886–905. 8

[5] Berenger, J. A perfectly matched layer for the absorbtion of electromagnetic waves. *Journal of Computational Physics 114* (1994), 185–200. 4

[6] Cerjan, C., Kosloff, D., Kosloff, R., and Reshef, M. A nonreflecting boundary condition for discrete acoustic and elastic wave equations. *Geophysics 50*, 4 (April 1985), 705–708. 4

[7] Dablain, M. High-order finite differences. *Geophysics 58* (1986). 7

[8] Davis, T. A., and Duff, I. S. An unsymmetric-pattern multifrontal method for sparse *LU* factorization. *SIAM Journal on Matrix Analysis and Applications 18*, 1 (1997), 140–158. 8

[9] Davis, T. A., Gilbert, J. R., Larimore, S. I., and Ng, E. G. Algorithm 836: Colamd, a column approximate minimum degree ordering algorithm. *ACM Trans. Math. Softw. 30*, 3 (2004), 377–380. 8

[10] Demmel, J. W., Eisenstat, S. C., J. R. G., Li, X. S., and Liu, J. W. H. A supernodal approach to sparse partial pivoting. *SIAM Journal on Matrix Analysis and Applications 20*, 3 (1999), 720–755. 1, 8

[11] Dessa, J.-X., and Pascal, G. Combined traveltime and frequency-domain seismic waveform inversion : a case study on multi-offset ultrasonic data. *Geophysical Journal International 154* (2003), 117–133. 2, 4, 7, 8

[12] Engquist, B., and Majda, A. Absorbing boundary conditions for the numerical simulation of waves. *Mathematical Computation 31* (1977), 629–651. 4, 17

[13] Erlangga, Y., Oosterlee, C., and Vuik, C. A novel multigrid preconditioner for heterogeneous helmholtz problems. Tech. rep., Delft University of Technology, 2004. 4, 7, 9

[14] Erlangga, Y., Vuik, C., and Oosterlee, C. On a class of preconditioners for solving the helmholtz equation. *Applied Numerical Mathematics 50* (2004), 409–425. 3, 4, 7, 9

[15] Erlangga, Y., Vuik, C., Oosterlee, C., Plessix, R., and Mulder, W. A robust iterative solver for the two-way wave equation based on a complex shifted-laplace operator. In *SEG International Exposition and 74th Annual Meeting* (2004), Society For Exploration Geophysics. 7

[16] George, A., and Liu, J. *Computer solution of large sparse positive definite systems*. Prentice Hall Inc., 1981. 1, 8

[17] George, J., and Liu, W. The evolution of the minimum degree algorithm. *SIAM Review 31*, 1 (1989), 1–19. 8

[18] Gupta, A. Recent advances in direct methods for solving unsymmetric sparse systems of linear equations. *ACM Transactions on Mathematical Software 28*, 3 (2002), 310–324. 8

[19] Hustedt, B., Operto, S., and Virieux, J. A multi-level direct-iterative solver for seismic wave propagation modelling: space and wavelet approaches. *Geophysical Journal International 155* (2003), 953–980. 7, 8, 9

[20] Hustedt, B., Operto, S., and Virieux, J. Mixed-grid and staggered-grid finite-difference methods for frequency-domain acoustic wave modellin. *Geophysical Journal International 157* (2004), 1269–1296. 4, 7, 8

[21] Jo, C., Shin, C., and Suh, J. An optimal 9-point, finite-difference, frequency-space 2d scalar wave extrapolator. *Geophysics 61*, 2 (1996), 529–537. 4, 7, 12

[22] Kelly, K., Ward, R., and amd R. Alford, S. T. Synthetic seismograms, a finite-difference approach. *Geophysics 41*, 1 (1976), 2–27. 1

[23] Kjartansson, E. *Attenuation of seismic waves in rocks and applications in energy exploration.* PhD thesis, Stanford University, 1979. 4

[24] Mora, P. Elastic wave-field inversion of reflection and transmission data. *Geophysics 53*, 6 (1988), 750–759. 2

[25] Mufti, I., Pita, J., and Huntley, R. Finite-difference depth migration of exploration-scale 3-D seismic data. *Geophysics 61*, 3 (1996), 776–794. 1

[26] Pitarka, A. 3D elastic finite-difference modeling of seismic motion using staggered grids with nonuniform spacing. *Bulletin Of The Seismological Society Of America 89*, 1 (1999), 54–68. 1

[27] Plessix, R. E., and Mulder, W. A. Separation-of-variables as a preconditioner for an iterative helmholtz solver. *Appl. Numer. Math. 44*, 3 (2003), 385–400. 7, 9

[28] Pratt, R. Frequency-domain elastic wave modeling by finite differences: a tool for crosshole seismic imaging. *Geophysics 55*, 5 (1990), 626–632. 1, 7

[29] Pratt, R. Seismic waveform inversion in the frequency domain, part 1: theory and verification in a physical scale model. *Geophysics 64*, 3 (1999), 888–901. 2, 7, 8

[30] Pratt, R., and Goulty, N. Combining wave-equation imaging with traveltime tomography to form high-resolution images from crosshole data. *Geophysics 56*, 2 (1991), 208–224. 2, 7

[31] Pratt, R., and Shipp, R. Seismic waveform inversion in the frequency domain, part 2: fault delineation in sediments using crosshole data. *Geophysics 64*, 3 (1999), 902–914. 2

[32] Pratt, R., and Worthington, M. Inverse theory applied to multi-source cross-hole tomography. Part 1: Acoustic wave-equation method. *Geophysical Prospecting 38* (1990), 287–310. 1, 2, 3, 4, 7

[33] Pratt, R., and Worthington, M. Inverse theory applied to multi-source cross-hole tomography. Part 2: Elastic wave-equation method. *Geophysical Prospecting 38* (1990), 311–330. 1, 2, 7

[34] Ravaut, C., Operto, S., Improta, L., Virieux, J., Herrero, . A., and Dell'Aversana, P. Multiscale imaging of complex structures from multifold wide-aperture seismic data by frequency-domain full-waveform tomography: application to a thrust belt. *Geophysical Journal International 159* (2004), 1032–1056. 2, 7, 8

[35] Saad, Y., and Schultz, M. H. Gmres: a generalized minimal residual algorithm for solving nonsymmetric linear systems. *SIAM J. Sci. Stat. Comput. 7*, 3 (1986), 856–869. 9

[36] Saenger, E., and Bohlen, T. Finite-difference modeling of viscoelastic and anistropic wave propagation using the rotated staggered grid. *Geophysics 69*, 2 (2004), 583–591. 1

[37] Sirgue, L., and Pratt, R. Efficient waveform inversion and imaging : A strategy for selecting temporal frequencies. *Geophysics 69*, 1 (2004), 231–248. 3, 4

[38] Song, Z., and Williamson, P. Frequency-domain acoustic-wave modeling and inversion of crosshole data: Part 1–2.5-d modeling method. *Geophysics 60*, 3 (1995), 784–795. 4

[39] Song, Z., Williamson, P., and Pratt, R. Frequency-domain acoustic-wave modeling and inversion of crosshole data: part ii- inversion method, synthetic experiments, and real-data results. *Geophysics 60*, 3 (1995), 796–809. 2, 4

[40] Stekl, I., and Pratt, R. Accurate viscoelastic modeling by frequency-domain finite differences using rotated operators. *Geophysics 63*, 4 (1998), 1779–1794. 7, 8

[41] Tang, J. Construction of a combined preconditioner for the helmholtz problem. Master's thesis, Delft University of Technology, 2004. 3, 7, 9

[42] Tarantola, A. Inversion of seismic reflection data in the acoustic approximation. *Geophysics 49* (1984), 1259–1266. 3

[43] Tarantola, A. Linearized inversion of seismic reflection data. *Geophysical Prospecting 32* (1984), 998–1015. 2, 3

[44] van der Vorst, H. A. Bi-cgstab: a fast and smoothly converging variant of bi-cg for the solution of nonsymmetric linear systems. *SIAM J. Sci. Stat. Comput. 13*, 2 (1992), 631–644. 9

[45] Villarreal, A., and Scales, J. Distributed three-dimensional finite-difference modeling of of wave propagation in acoustic media. *Computers in Physics 11*, 4 (1997), 388–389. 1, 2

[46] Watanabe, T., Nihei, K., Nakagawa, S., and Myer, L. Viscoacoustic wave form inversion of transmission data for velocity and attenuation. *Journal of the Acoustical Society of America 115*, 6 (2004), 3059–3067. 2, 4, 7, 8

[47] Williamson, P. A guide to the limits of resolution imposed by scattering in ray tomography. *Geophysics 56*, 2 (1991), 202–207. 1

[48] Yannakakis, M. Computing the minimum fill-in is np-complete. *SIAM Journal on Algebraic and Discrete Methods 2*, 1 (1981), 77–79. 8

[49] Yokota, T., and Matsushima, J. Seismic waveform tomography in the frequency-space domain: selection of the optimal temporal frequency for inversion. *Exploration Geophysics 35* (2004), 19–24. 4